We are IntechOpen, the world's leading publisher of Open Access books Built by scientists, for scientists

4,800
Open access books available

122,000
International authors and editors

135M
Downloads

154
Countries delivered to

Our authors are among the

TOP 1%
most cited scientists

12.2%
Contributors from top 500 universities

CLARIVATE ANALYTICS
BOOK CITATION INDEX
INDEXED

WEB OF SCIENCE™

Selection of our books indexed in the Book Citation Index
in Web of Science™ Core Collection (BKCI)

Interested in publishing with us?
Contact book.department@intechopen.com

Concrete Microstructure Characterization and Performance

Cristian Druta

Abstract

Microstructural characteristics such as the interfacial transition zone (ITZ) and cracking patterns from compressive strength testing are main features that characterize concrete behavior. Certain materials such as blast furnace slag or fly ash introduced in the concrete mix aid in improving its strength and durability. Others such as nanosilica particles may affect only the microstructure of the paste without making any significant improvement in the strength of the ITZ or paste-aggregate bond. Additionally, in situ investigation of the microstructures of fresh cement paste can greatly enhance knowledge of the development properties of concrete at an early age (e.g., setting and hydration), which can be helpful for improvement of the quality of concrete. Common technologies such as Scanning Electron Microscope (SEM) are currently employed in petrographic analysis of cementitious materials and concrete microstructure.

Keywords: microstructure, damage, interface, compressive strength, transition zone

1. Introduction

Although the technology of producing concrete is relatively simple the microstructure of the resultant product is highly complex. Concrete microstructure is defined as the microscopical detailing of the concrete components from its macrostructure. To better understand the mechanisms that intrinsically control durability of Portland cement concrete (PCC) it is necessary to define and understand those factors affecting concrete microstructure. Typically, the microstructure is a consequence of both the concrete formulation and the processes taking place during mixing, placing and curing. Past studies have already established that deterioration originates in the concrete at the micro- or sub-microscopic level, i.e., in its microstructure [1, 2].

Several current studies on concrete failure indicated that an often major cause of variability of the properties and performance of the hardened concrete was the inadequate dispersion of cement paste in the fresh concrete [3]. In this way, harmful impurities that permeate or diffuse throughout the hardened concrete may initiate its deterioration due to a variation in the ability of the concrete to restrict their transport. Moreover, the cement particles tend to irregularly coagulate and cluster in the mix leading to uneven regions of dense and high porosity hardened paste because of poor dispersion and inhomogeneity during mixing and placing. This holds true even for high density microstructures resulting when using of low

water/cement (w/c) ratios. The development of a dense homogeneous microstructure is also affected by the pattern packing of the cement particles and aggregate. Thus, the microstructure developed during the mixing, setting and hardening process will directly affect the resulting properties and performance of concrete. Microstructural development is also controlled by a combination of uniform dispersion of cement particles, mineral admixtures and aggregates along with cement hydration. Moreover, developments occurring at a micro- or sub-microscopic level in the concrete matrix influence aspects such as early or retarded setting, drying shrinkage, permeability, frost damage, excessive bleeding, and/or inadequate strength. Understanding the concrete behavior at these small scale levels is the initial and most important step toward achieving the means to control its microstructure and influence on performance [3].

Additionally, the examination of concrete microstructure either in transmitted or reflected energy is a valuable tool in the study of concrete microstructure. These methods can be used in inspecting various concrete specimens to determine potential defects or material characteristics. For example, water/cement ratios can be determined by comparing paste porosity with a series of carefully prepared reference samples. In this chapter, the physical interface between aggregate and cement paste and the aggregate fracture were studied. The Scanning Electron Microscope (SEM) capable of acquiring micro-scale level images was used to quantify the ITZ cracking for normal and self-consolidating concrete. The X-ray Computed Tomography (CT) system was employed to visualize the coarse aggregate distribution in the concrete specimens and their fracture pattern. SEM is a device that creates highly magnified 2-D images of structures to analyze their various components interactions and potential flaws using accelerated electrons. The X-ray CT technique uses high energy beams which penetrate samples of different thicknesses then stacks up the acquired images to reconstruct a 3-D model of the scanned sample for structural analysis.

2. Research methodology

The first part of this section addresses the development of microstructure and its control of performance with a focus on the normal (NC) and self-consolidating concrete (SCC). The second part details the damage caused by steel projectiles of different sizes impacting large concrete specimens at various speeds.

2.1 Concrete microstructure characterization and performance comparison

This research study had four objectives: (1) To investigate the bonding between coarse aggregates and cement paste; (2) To evaluate fresh SCC test methods – slump flow and U-tube; (3) To compare NC and SCC splitting tensile strength and compressive strength; and (4) To visualize the distribution of coarse aggregate in NC and SCC concrete specimens. The SEM imaging was employed to investigate the bonding between the cement paste and coarse aggregate of the two types of concrete by studying their interfacial transition zone (ITZ). The ITZ, which is mostly comprised of calcium hydroxide, is a narrow and fuzzy cement paste area surrounding the aggregate particles. Being a very porous region due to a high water content, the ITZ tends to increase with the aggregate size. Moreover, due to its weaker structure compared to the bulk paste in the concrete this transition zone directly affects the concrete properties, especially its strength and stiffness. The aggregate distribution throughout the specimens and the fracture patterns of the NC and SCC specimens tested for compressive strength were visualized using the

X-ray tomography imaging system. The standard compressive strength test method depicts typical fracture patterns indicative of the mix strength or existing problems with the testing equipment.

Additional information on materials and admixtures used for preparing the specimens can be found in Druta et al. [4]. **Table 1** presents the mix proportions for casting the SCC specimens. The type I Portland cement was replaced by blast furnace slag (25%), fly ash (15%), and silica fume (5%). Similar mix proportions and equal amount batches were prepared for casting cylindrical NC samples and conduct slump tests without incorporating any mineral admixtures.

W/C ratio	Water (kg)	Cement (kg)	Fine Agg. (kg)	Coarse Agg. (kg)	HRWR (ml)	VMA (ml)
0.3	3	5.5	16.3	21.1	340	0
0.4	4	5.5	16.3	21.1	100	15
0.45	4.5	5.5	16.3	21.1	80	25
0.5	5	5.5	16.3	21.1	50	50
0.6	6	5.5	16.3	21.1	20	100

Table 1.
Self-consolidating concrete mix design.

Splitting tensile and compressive strength tests were performed on both types of concrete, whereas U-box and slump flow tests were conducted to evaluate the filling ability and the self-compactability of the SCC, respectively [5, 6]. The slump flow test, currently used for fresh SCC, is a good indicator of concrete consistency and ability to self-consolidate [6, 7]. For SCC, instead of measuring the drop in height of the fresh concrete the average of two perpendicular diameters (R1 and R2) of the spread concrete is determined. A good self-consolidation is achieved for a spread of 600 mm or larger, up to 800 mm, within a time period of 60 s [4]. **Figure 1** illustrates the filling ability apparatus that comprises an approximately 700 mm tall tube with a round bottom divided into two equal sections by a middle wall incorporating a sliding gate. Once the left section is filled with concrete the sliding gate is lifted allowing the fresh concrete to flow freely in the right section through a specially designed grate provided with closely spaced rebars. The height levels of the concrete in both sections are measured, then followed by a height difference calculation. An adequate SCC filling and compactability is achieved if a difference of 30 mm or less between H1 and H2 is recorded.
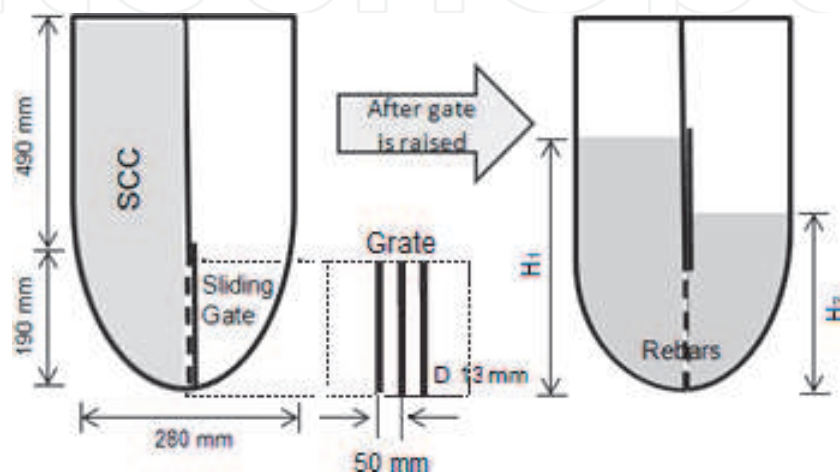

Figure 1.
U-box schematic for testing SCC.

2.2 Evaluating the bond between coarse aggregate and cement paste

The SCC was extensively researched in the past decades to find ways to enhance its performance [8, 9]. The general focus of those efforts was the improvement of the interface properties between paste and aggregates. That improvement has led to the manufacturing and use of higher strength and enhanced durability concretes [10, 11]. The physical interface between aggregate and cement paste and the aggregate fracture patterns were investigated in the second phase of this study. First, the ITZ cracking behavior for the two types of concrete was quantified using the SEM capable of acquiring micro-scale level images. Secondly, a visualization of the coarse aggregate distribution in the specimens and their fracture pattern were performed by employing the X-ray Computed Tomography (CT) system [2]. In addition, a comparison of the number of air voids in the NC and SCC was conducted on six rectangular samples with the dimensions of $70 \times 70 \times 12$ mm. The samples were cut from concrete cylinders at 0.3, 0.45, and 0.6 water-cement ratios and analyzed under a digital stereo-zoom microscope.

To determine the characteristics of the interfaces between aggregates and paste for both SCC and NC, small samples of 25.5 mm diameter and 4 mm thick were obtained from untested cylinders of both types of concretes at three different
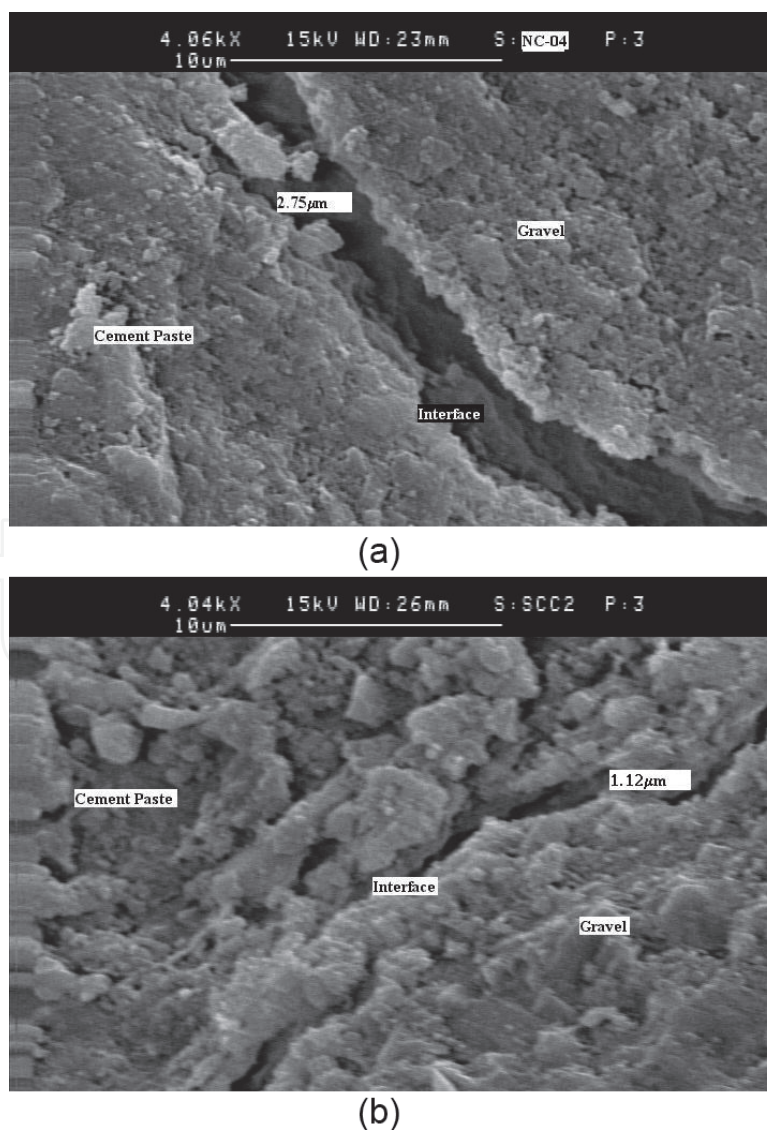

(a)

(b)

Figure 2.
Photomicrographs of (a) normal concrete and (b) self-consolidating concrete physical interfaces (w/c = 0.40).

water-cement ratios of 0.3, 0.4, and 0.6 after 60 days of curing. The SEM was used to capture pictures of each w/c ratio sample at different ITZ locations. Smaller crack widths within their physical interface were observed from the acquired SEM photomicrographs for SCC samples compared the NC samples as showed in **Figure 2**. This finding indicated that a better aggregate-paste bonding was achieved in the transition zone for SCC compared to NC.

The use of silica fume led to a lower porosity and less growth of calcium hydroxide in the ITZ resulting in an increase in tensile and compressive strength of the SCC when compared to NC. Typically, silica fume has a "filler effect" in the concrete structure that reduces internal bleeding in the fresh concrete while enhancing the aggregate-paste bond strength [12]. It also renders its structure more homogeneous due to a reduction of the large pores in the ITZ. The split tensile strength tests revealed a larger number of broken aggregate particles in SCC than in NC when the fractured surfaces of the concrete samples were inspected. Furthermore, the strength of the ITZ was also enhanced by the addition of silica fume, as some of the aggregate fracture occurred at the physical interface instead within the transition zone.

Table 2 shows the specimens' cracks widths from the images acquired at each water/cement ratio. The SEM image analysis indicated that a tendency for the cracks to shrink existed for lower w/cm ratios. However, a certain relationship between the interface crack widths and the water-cement ratios for either type of concrete was not found. Establishing a quantitative relationship between the crack width and strength, if any, has to be further investigated.

w/c ratio	NC width range (μm)	SCC width range (μm)
0.3	0.62–1.75	0.01–0.75
0.4	0.63–5.63	0.01–1.12
0.6	1.23–3.38	0.01–0.61

Table 2.
Interfaces crack widths for normal and self-consolidating concretes.

2.3 Analysis of fracture patterns

The X-ray computed tomography (CT) was employed to examine the internal structure and fracture patterns of the concrete specimens tested in compression [4]. Using the CT radiographic inspection technique objects are reconstructed from their cross sectional images. Over the years, nondestructive evaluations using CT imaging of the microstructure of concrete [13], soil [14, 15], rock [16], and asphalt concrete [17, 18] have been largely used. Compression tested specimens have exhibited similar fracture patterns, i.e., cone at one end and vertical columns, as types 2 and 3 patterns described in the ASTM C 39 test method. **Figure 3** shows tomographic images of the 3D reconstructed SCC and NC specimens acquired from the top, middle and bottom. Images reveal concrete structural damage and fracture patterns along with the aggregate fracture throughout the tested specimens. The SCC specimens did not exhibit any segregation.

Several sectional images of 100 × 200 mm tensile split cylindrical specimens were visually inspected to identify fractured aggregate. The analysis showed that the percentage of fractured aggregate for SCC was about 15–25% (9–15 out of 60) while for NC was around 10% (4–6 out of 60) after determining that each section facet contained around 60 coarse aggregate particles. The number of broken aggregate particles from three tested specimens was averaged to calculate the fracture
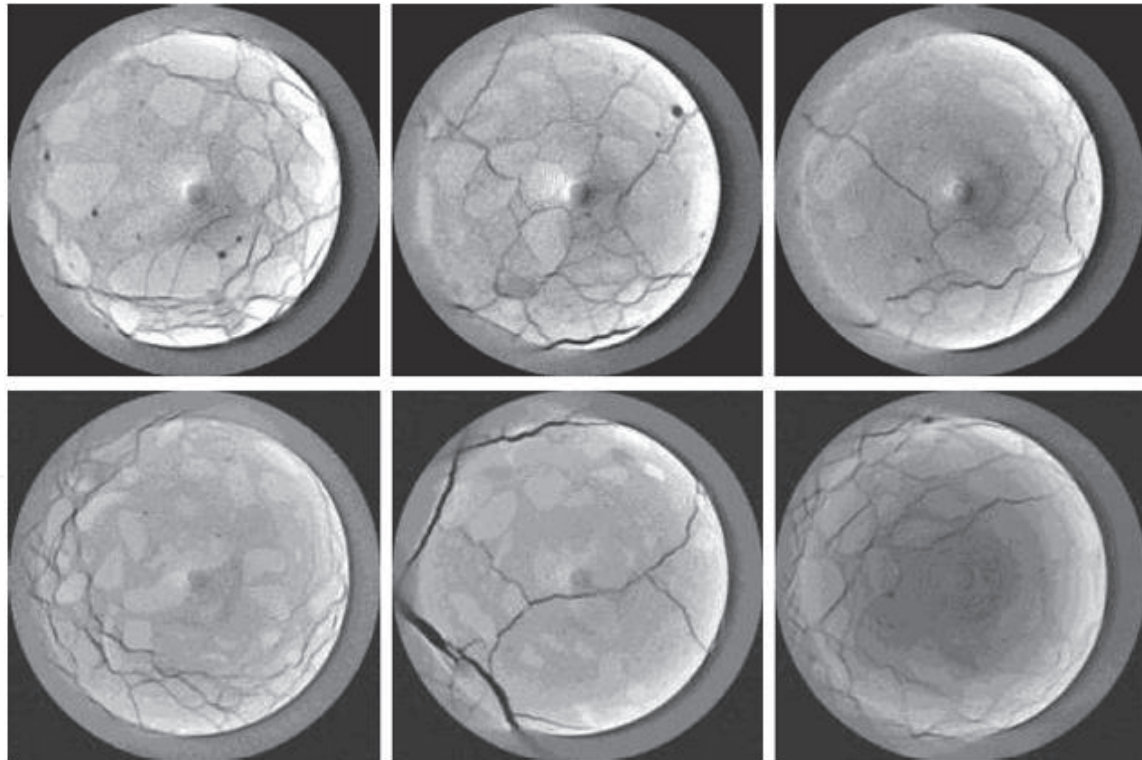
Figure 3.
Tomographic images of SCC (top row) and NC (bottom row) specimens after being tested in compression (from left to right: top, middle, and bottom of specimen).

percentages. The greater number of fractured aggregate in the SCC specimens was another indication of a better bonding between aggregate and cement paste.

2.4 Evaluation of air void content

The air entrainment was reduced in the SCC mix with the addition of finely divided mineral admixtures, such as fly ash and silica fume. Samples with the dimensions of 80 × 80 × 12 mm were acquired from both types of concretes at w/cm ratios of 0.30, 0.45, and 0.60 to study their air-entrained properties. Air voids larger than 200 microns only were considered for the analysis. The measurements showed that SCC samples exhibited half the amount of air voids compared to NC. Visual analyses of the "air voids" sizes and shapes revealed that SCC had smaller and more round-shaped voids than NC which presented slightly larger and irregular shaped voids (by 15–20%) (**Figure 4**).
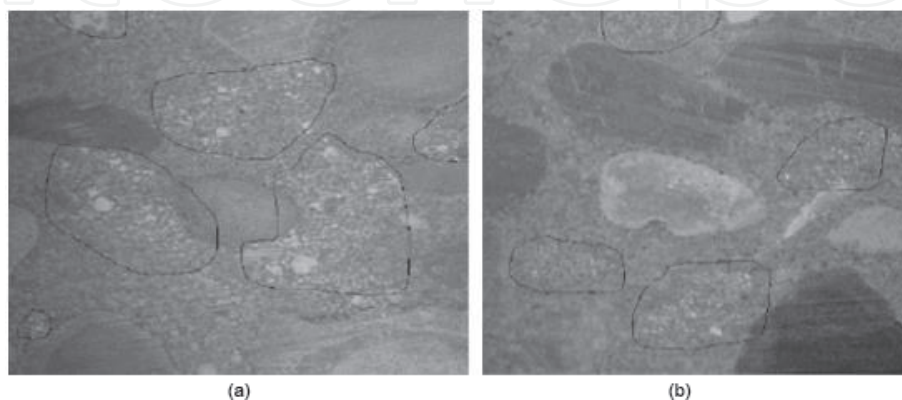

(a)   (b)

Figure 4.
Distribution of air voids (white spots) in: (a) NC and (b) SCC.

Moreover, while the air voids in the SCC appeared more clustered in certain areas of the cut specimen, the voids in NC were relatively well dispersed in the

specimens. These data indicate that the lower air void content also contributed to an increase in strength of the SCC as cracks initiate more easily in the cement paste with higher air voids. Some of these air voids represent "flaws" in the cement paste at the aggregate-paste boundary possibly forming microcracks or "bond cracks" in the ITZ which ultimately lead to the failure of the concrete due to the propagation of microcracks under localized tensile stresses.

2.5 Conclusions

This research verified that SCC achieved self-compactability and adequate flow under its own weight, without external vibration or compaction based on the mix proportion parameters and the materials used. The study also showed that splitting tensile and compressive strengths in SCC were higher than those of normal vibrated concrete due to the addition of chemical and mineral admixtures. Compressive strength had an average increase of over 60%, whereas the splitting tensile strength showed a 30% increase. The ratio between the splitting and compressive strength was similar to values found in the literature. Also, a better bonding between aggregate and cement paste was achieved in SCC due to the use of chemical and mineral admixtures, as the material has shown smaller aggregate-matrix interface microcracks than normal concrete. This characteristic affected both the splitting tensile and compressive strengths. Another indicator of the stronger aggregate-paste bonding was the greater percentage of the fractured aggregate in SCC (20–25%) compared to the 10% for normal concrete. Moreover, when compared to NC, the number of air voids in SCC was lower and they appeared relatively smaller and more rounded. These factors have contributed as well to the increase in strength of the SCC.

3. Concrete microstructure damage by projectile impact

Penetration of projectiles into concrete target was investigated in this research by using both experimental and simulation methods. The over-all objectives of the project included: (a) Building up an experimental facility to conduct the penetration test; (b) Developing of a rational constitutive model to incorporate distributed damage effects; (c) Enhancing of the model implementation by combining the Finite Element Method (FEM) and the Discrete Element Method (DEM) so that post-fracture behavior can be simulated; and (d) Developing of methods to back-calculate model constants from comparing experimental with simulation results.

Figure 5.
Gas operated facility for testing concrete samples.

The equipment assembled for testing concrete specimens of different sizes and strengths is showed in **Figure 5**. It contains a gas tank that can be filled at various pressures, a launch tube, a gas expansion tank, and specimen housing chamber.

A three-dimensional penetration model was constructed using ABAQUS as shown in **Figure 6**. The concrete target was tentatively modeled as 40 × 40 × 100 cm blocks and penetrated by high speed projectiles made of rigid materials. No deformation is assumed for the projectile when penetrating the target. The concrete is assumed to be an elasto-plastic material with damage property. 8-node linear brick elements are used for the FEM mesh. An unbounded boundary domain is defined by using 8-node linear infinite elements, which are connected with concrete specimen at the periphery (**Figure 6**).
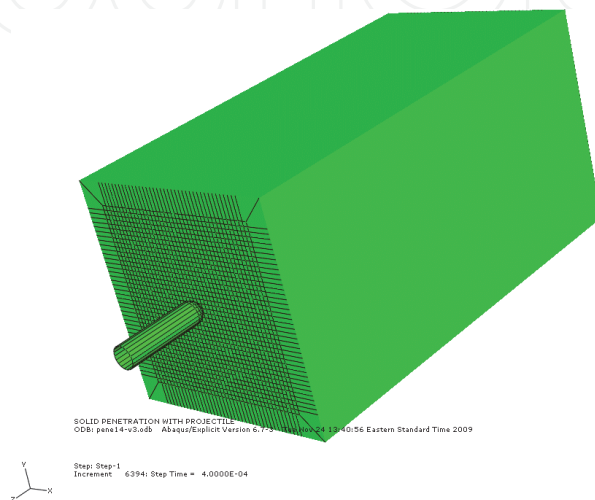

Figure 6.
FEM modeling of concrete target impacted by projectile.

The microstructure of concrete specimen is considered by assigning different material properties to the three components of the mixture, aggregate, mortar (hydration products plus fine aggregate particles) and air void. These components are discriminated by utilizing image analysis techniques shown in **Figure 7(a)** and **(b)**. Pixel intensity value determines what component each pixel belongs to. When meshing the domain to be modeled, the properties of the material between two scanned images are assumed to be the same as the front image.

3.1 Concrete damage

A reduction in the elastic stiffness of concrete is the result of damage typically associated with the failure mechanisms of the concrete (cracking and crushing). According to the scalar-damage theory, the isotropic stiffness degradation is characterized by a single degradation variable, *d*. Based on continuum damage mechanics notions, the effective stress is defined as Eq. (1).

$$\overline{\sigma} = D_0^{el} : \left(\varepsilon - \varepsilon^{pl}\right) \tag{1}$$

The Cauchy stress is related to the effective stress through the scalar degradation relation per Eq. (2).

$$\sigma = (1 - d)\overline{\sigma} \tag{2}$$

The stress-strain relations are governed by scalar damaged elasticity given in Eq. (3), where D_0^{el} is the elastic stiffness of the undamaged material; $D^{el} = (1 - d)$
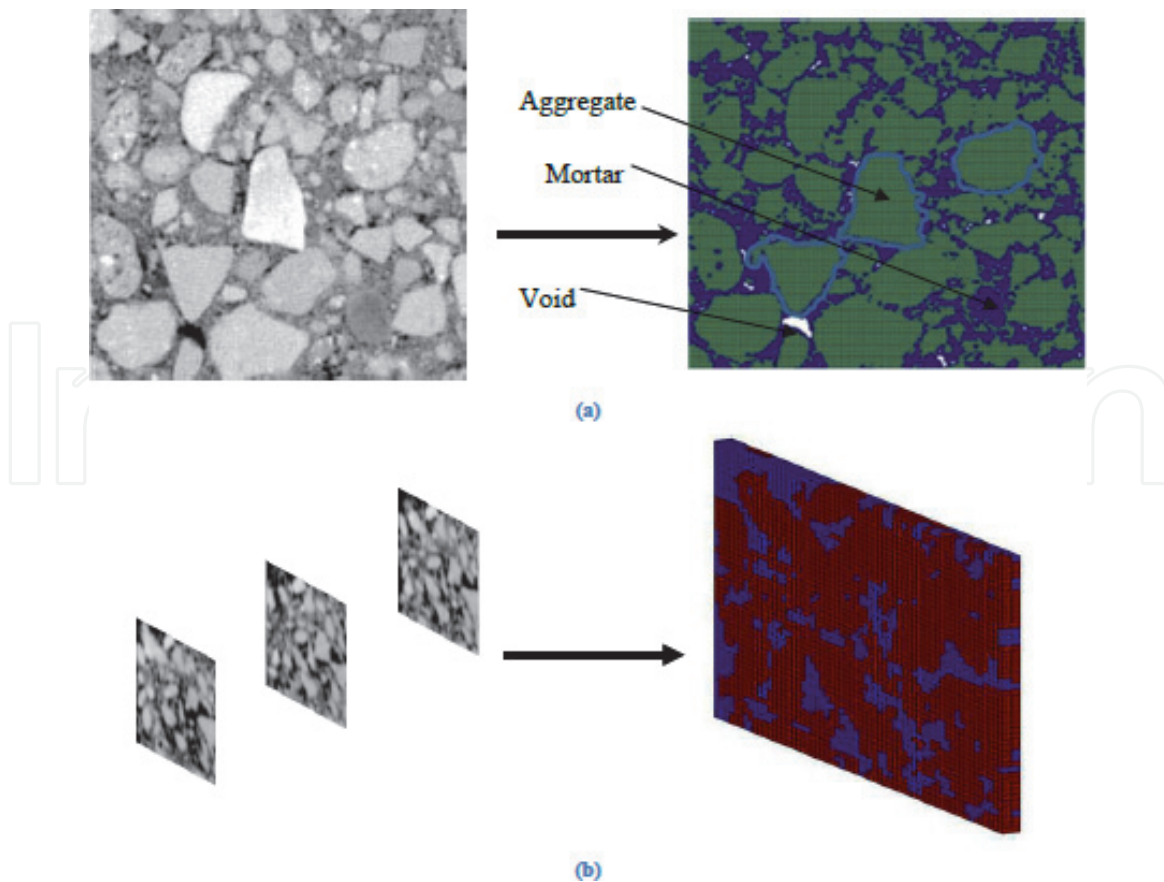
Figure 7.
3D microstructure of concrete specimen (a) and the image-based reconstruction (b).

D_0^{el} is the elastic stiffness due to damage; and d is the scalar stiffness variable due to degradation. A d value of zero indicates undamaged material while one shows a fully damaged material.

$$\sigma = (1 - d)D_0^{el} : \left(\varepsilon - \varepsilon^{pl}\right) \tag{3}$$

The constitutive behavior of concrete was illustrated using the concrete damaged plasticity model. The model describes the inelastic behavior of concrete based on the concepts of isotropic damaged elasticity in combination with isotropic tensile and compressive plasticity. Moreover, the scalar damaged elasticity combined with the non-associated multi-hardening plasticity describe the irreversible damage that occurs during the fracturing process. The main ingredients of the model are summarized below.

3.2 Strain rate decomposition

Additive strain rate decomposition is assumed for the rate-independent model according to Eq. (4).

$$\dot{\varepsilon} = \dot{\varepsilon}^{el} \text{ (elastic)} + \dot{\varepsilon}^{pl} \text{ (elastic)} \tag{4}$$

For any given cross-section of the material, the ratio of the effective load-carrying area (i.e., the total area minus the damaged area) to the overall section area is represented by the $(1 - d)$ factor. Thus, the effective stress is equivalent to the Cauchy stress, σ, if there is no damage, $d = 0$. When damage occurs, however, the effective stress is larger than the Cauchy stress because the external loads are supported by the effective stress area. Therefore, the plasticity problem can be

conveniently formulated using the effective stress component. The development of the degradation variable is governed by a set of hardening variables, $\tilde{\varepsilon}^{pl}$ (plastic strains), and the effective stress, $d = \mathrm{d}(\bar{\sigma}, \tilde{\varepsilon}^{pl})$.

3.3 Hardening variables

Two hardening variables, $\tilde{\varepsilon}_t^{pl}$ and $\tilde{\varepsilon}_c^{pl}$, defined as equivalent plastic strains in tension and compression, respectively, can be used to independently characterized a material damaged states in tension and compression. Generally, increasing values of the hardening variables may lead to microcracking and crushing in concrete. These variables also control the degradation of the elastic stiffness and the progression of the yield surface, as well as affecting the dissipated fracture energy required to generate microcracks.

Also, a yield function, $\mathrm{F}(\bar{\sigma}, \tilde{\varepsilon}^{pl})$, that represents a surface in effective stress space, will determines the states of failure or damage. For the inviscid plastic-damage model, it is represented by Eq. (5).

$$\mathrm{F}\left(\bar{\sigma}, \tilde{\varepsilon}^{pl}\right) < 0 \tag{5}$$

4. DEM modeling

Penetration test is also modeled using the Discrete Element Method (DEM). DEM was first introduced by Cundall [19] in the early 1970s. It was originally applied on rocks, then extended to granular material, which triggered much wider uses in different kinds of material like fluid, soil, and composites. DEM has not received much attention in penetration simulation before 1990. Before 1990, Heuze's overview [20, 21] indicated that only 3 computer programs based their theory on DEM. However, DEM has its intrinsic advantages, especially related to penetration simulation, when compared to other numerical simulation methods, such as FEM-based on continuum meshing. DEM allows transitioning from continuum to discontinuum to be easily simulated, while handling fracturing and large deformation conveniently.

The geometry of a projectile is one of the key factors affecting the penetration process. A number of studies have addressed the shape effects including those on flat nose [22–24], ogive [25], and spherical ball [26]. Zhu and Zhang [27] compared the effects on penetration using projectiles of ogive and flat nose shape. While most researchers consider projectiles as rigid, others investigated the effects due to a deformable projectile. As for the impact velocity, Nishida [26] studied the penetration at a low velocity of 16 m/s while most others focused on velocities larger than 100 m/s.

DEM is also used in the theoretical formulation of PFC3D (a particle modeling software) known as particle-flow model. Particles of arbitrary shapes that displace independent of each other and occupy a finite amount of space constitute the basic element of the model. The model uses a finite normal stiffness to represent the contact stiffness, while the interaction between the particles, which are assumed rigid, is defined using a soft contact approach. Force-Displacement Law and Motion Law are the two primary rules to define the mechanical computation. The former law is used to calculate the contact force and momentum between two entities based on their relative displacement. It should be noted that the momentum part could only be modeled in the parallel bond model for contacts. The second law, also referred as Newton's second law, governs how force and momentum determine the particle translational and rotational motion.

4.1 Projectile model

In order to build the required cone shape mono-size balls are decreased in size from tail to tip. To keep a compact status inside the projectile the overlap of balls and large stiffness were purposely assigned. The balls forming the projectile were clumped into one object using the PFC3Dclump function. The created object does not allow any relative movements for the balls constituting the projectile. The friction between projectile and the target varies with their relative velocity and is defined by Eq. (6), where the static friction was determined by using the idealized infinite velocity Chen [28].

$$f = f_{inf} + (f_{stat} - f_{inf})e^{\gamma * vel} \tag{6}$$

where f_{inf} is the friction with idealized infinite velocity and f_{stat} is the static friction.

Figure 8 illustrates a projectile model used to simulate penetration velocity versus depth relationship established by Forrestal et al. and their corresponding microscopic scale parameters. A model of a projectile created in PFC3D is showed in **Figure 9**. Most experiments use the cylindrical projectile shape which allows the convenient monitoring of symmetric damage. However, cubic specimens are used in simulations due to their simple geometry. By using large dimensions, the corner or boundary effects can be minimized. Although a semi-infinite target can be used in the classic penetration theory, a DEM simulation only accepts finite size targets, with its specific dimension needing to be determined to eliminate the size effect.
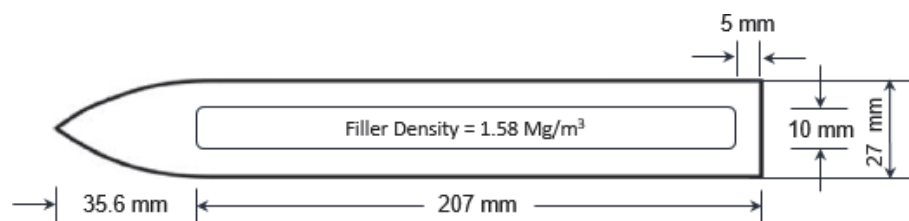

Figure 8.
Geometry of projectile used in test (Forrestal et al., 1994).

For both projectile and target, there are several major parameters contributing to the entire penetration process significantly. The major variables for projectile are mass (m), diameter (dia), nose shape, and impact velocity (vel). The former three are set in the projectile geometric and mechanical property file, while the last variable is input in the main code for penetration simulation. Key variables for target are macro Young's modulus (E), Poisson's ratio (ν), compressive strength (σ_c), and tensile strength (σ_t). They together represent the mechanical characteristics of the material.

PFC3D provides an optimized calibration sequence for some major control variables to minimize the iterations for parallel bond.

1. Matching the material's Young's modulus by varying E_c and $\bar{E}_c$.

2. Matching the Poisson's ratio by varying k_n/k_s and $\bar{k}_n/\bar{k}_s$.

3. Varying the mean normal and shear strength, $\bar{\sigma}_c$ and $\bar{\tau}_c$, as well as their standard deviation, to obtain the strength envelope for both compression and tension.

4. Properties, such as post-peak behavior or crack-initiation stress, can also be obtained by adjusting related variables, such as friction coefficient to match with those from the real samples; for conciseness purpose however, they are not presented in this paper.
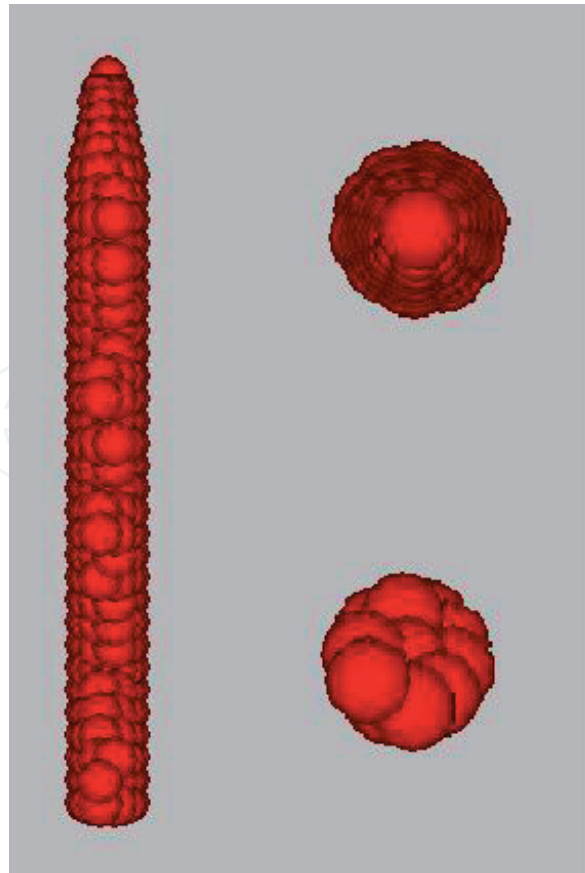
Figure 9.
Projectile model created in DEM.

4.2 Normal and shear strength calibration for parallel bond

Normal strength and shear strength ($\bar{\sigma}_c$ and $\bar{\tau}_c$) for parallel bond are the two major micro-parameters contributing to the material's compressive strength. Three typical calibration tests were carried out: varying normal strength, varying shear strength, and varying both with a constant relative ratio. The relationship between compressive strength and microstrength is shown in the **Figure 10**.
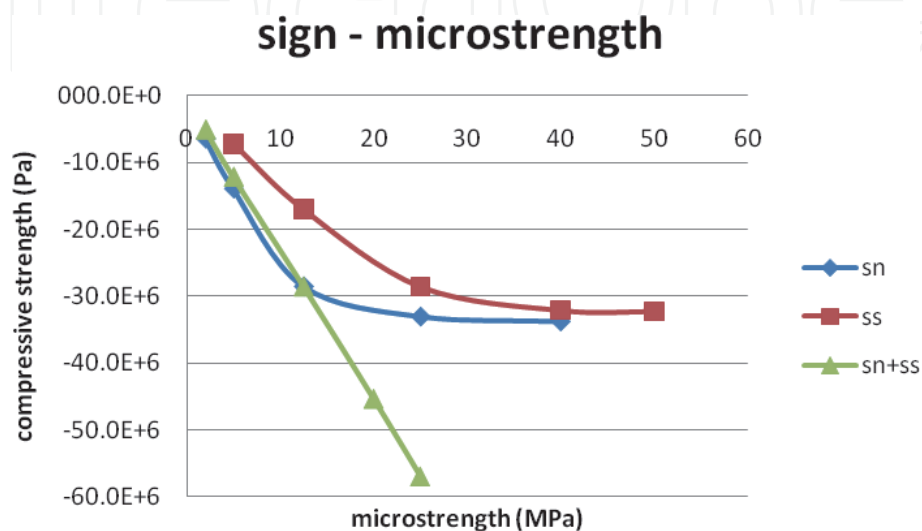

Figure 10.
Relation between macro-compressive strength and micro-strength.

As illustrated in **Figure 10**, the macro compressive strength depends on both normal and shear strength of the contact balls, while normal strength contributes a little more. An important feature for this case is that it is the smaller one of these two micro-parameters controls the upper limit of the macro-strength, i.e. the compressive strength cannot increase when either one of the micro strengths stay at a constant level.

For Young's modulus and Poisson's ratio, neither the normal nor the shear strength of particles has much contribution in the normal range. However, when both these two micro strengths decrease to very small values, the Young's modulus and Poisson's ratio have a little more influence.

The empirical discoveries found in the above calibration test can be used to form concrete target with the required mechanical property, although the calibration still needs to be conducted step by step. This is because different micro-variable changes may result in similar macro-property, and the changing magnitudes probably vary widely as other parameters vary.

5. Experimental results

Two types of concrete targets were made for penetration testing, i.e., the frusta of either a pyramid or a cone (**Figure 11**). The pyramid and cone shapes were intended to save materials in the rear end of the samples. The larger-area side was subjected to the projectile penetration. The frustum of pyramid had dimensions of 12″ × 12″ in the larger-end side and 13″ in depth, while the cylinders were 6″ and 11″ in diameter and 11″ in height. Both types of concrete targets were cast in 5000 psi and 8000 psi uniaxial compressive strengths. For verification purposes of the gas operated facility the first two shots were on two 2500 psi concrete cylinders (6″ × 12″). Limestone aggregate (#67) was used for the 5000 psi samples while (#78) was used for the 8000 psi samples.

Figure 11.
Types of concrete targets used for penetration testing.

Projectiles of three different diameters (12, 20, and 30 mm) were used for penetration into the concrete targets and were launched using the same pressures (1200 psi) to assess their speeds, penetration depths, and target damage.

Figure 12 shows an example of the projectile after impacting the concrete targets, the damaged concrete targets and location of projectiles after the impact. Some target specimens were shattered by the projectile and the penetration of the projectile were not observed. This was primarily due to the size of concrete specimen relative to that of the projectile. However, as projectile size decreases (or concrete specimen size increases), the phenomena of projectile penetrating through concrete target become more likely to occur.
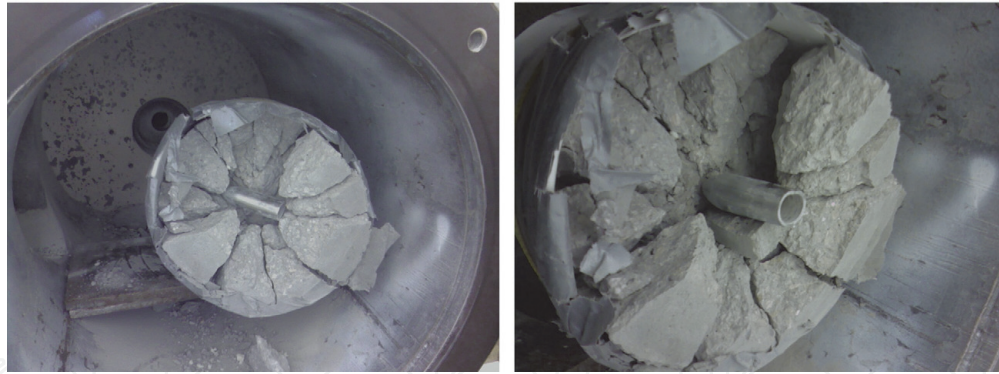
Figure 12.
8000 psi cylinder impacted by 30 mm diameter and 218 g projectile at v = 360 m/s.

5.1 Comparison between FEM simulation results and laboratory test results without considering the microstructure of the target

It is worth mentioning that both the mass and diameter of the projectiles influence the penetration depths. However, the major factor to determine the penetration depth is the velocity of the projectile. For example, in tests 7 and 8, the two projectiles have similar masses and diameters, but the projectile with higher velocity (405 m/s) has a penetration depth of 51 mm which is almost twice the depth of the one with lower velocity (360.5 m/s). This fact is also revealed by the simulation results, pertaining to the same tests, in which the projectile having a higher velocity has a 106 mm penetration depth, while the one with lower velocity has a 51 mm penetration depth. The major reason for the inconsistency between the simulation results and the test results is that the material properties including microstructure were not varied for different materials (**Table 3**).

Test #	Target type	Test penetration depth (mm)	Simulated penetration depth (mm)
1	Cyl (11″ × 11″)	80	84
2	Cyl (11″ × 11″)	96	83
6	Cyl (11″ × 11″)	87	150
7	Cyl (6″ × 12″)	27	18
8	Cyl (6″ × 12″)	51	106

Table 3.
Penetration depth comparison between test data and simulation (Zhou et al., 2009).

5.2 Comparison between simulation results and laboratory test results with microstructure incorporated for the concrete target

As previously mentioned, the 6″ × 12″ concrete cylinders were X-ray CT scanned and cross-section images showing their internal structure were obtained for each specimen. An image analysis code has been developed to reconstruct the internal structure of the target specimen using the x-ray CT slices. Thus, different constituents of concrete are identified respectively, based on the gray levels of a cross-section image. In addition to the reconstruction of the internal structure, the program also maps each pixel of the image onto the mesh of the digital model as shown in **Figure 13**. For each of the two 6″ × 12″concrete specimens, 100 slices
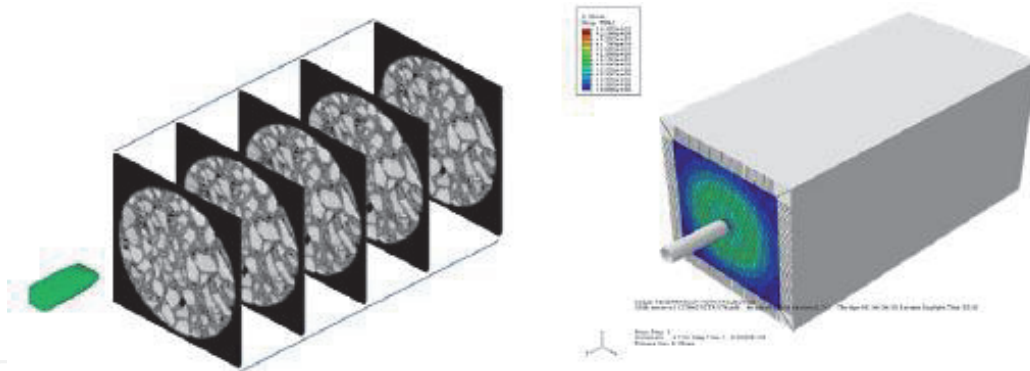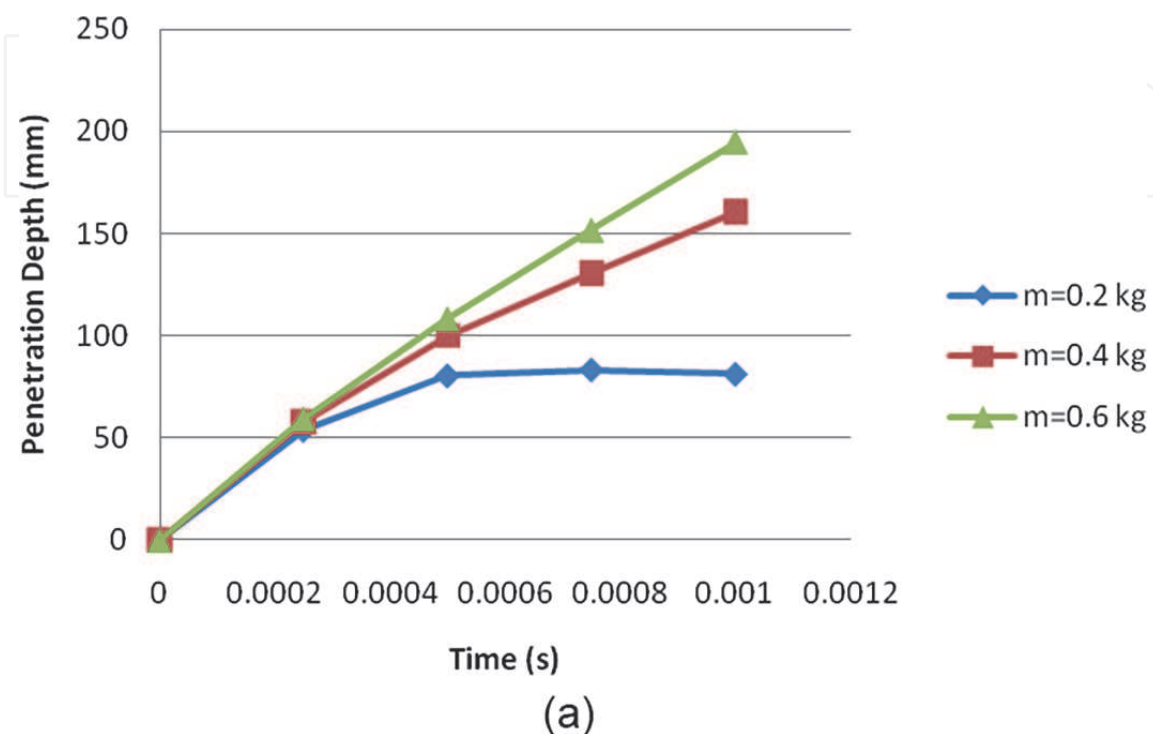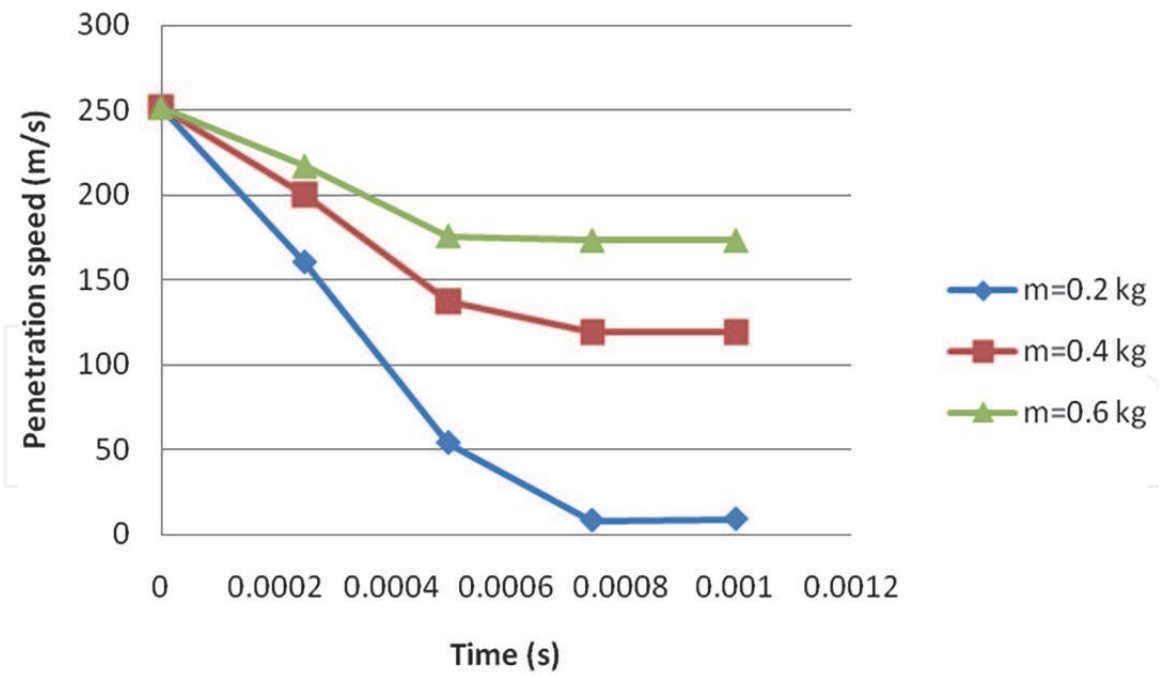
Figure 13.
Internal structure reconstruction of the concrete specimen.

(cross-section images) were stacked together and processed to generate their respective digital specimen. Elements pertaining to different components of the mixture (i.e., aggregates and cement paste) were assigned different material properties in the simulation. The aggregates were treated as elastic material with high elastic stiffness, whereas the cement paste was treated as an elasto-plastic material with low elastic stiffness and shear damage factor to control the damage of the material.

5.3 Effect of projectile mass on the simulated penetration

The effect of the projectile mass on the penetration was assessed by considering three different masses in the simulation – 0.2, 0.4, and 0.6 kg, respectively. Other properties of the projectiles were kept the same. The simulation data are presented in **Figure 14**. From the figure it can be noticed that the projectile penetration depth increases as its mass increases (a) whereas the penetration speed decreases at smaller rates for larger mass projectiles (b).

(a)

(b)

Figure 14.
Penetration depth and speed reduction of projectiles with different masses. (a) projectile penetration depth increases as its mass increases whereas (b) the penetration speed decreases at smaller rates for larger mass projectiles.

5.4 Visualization of DEM simulation

After creating the target and projectile models, it is convenient to assign different striking velocities to the projectile and perform penetration simulation. Through PFC3D coding, the entire penetration process can be simulated at selected time steps (**Figure 15**).
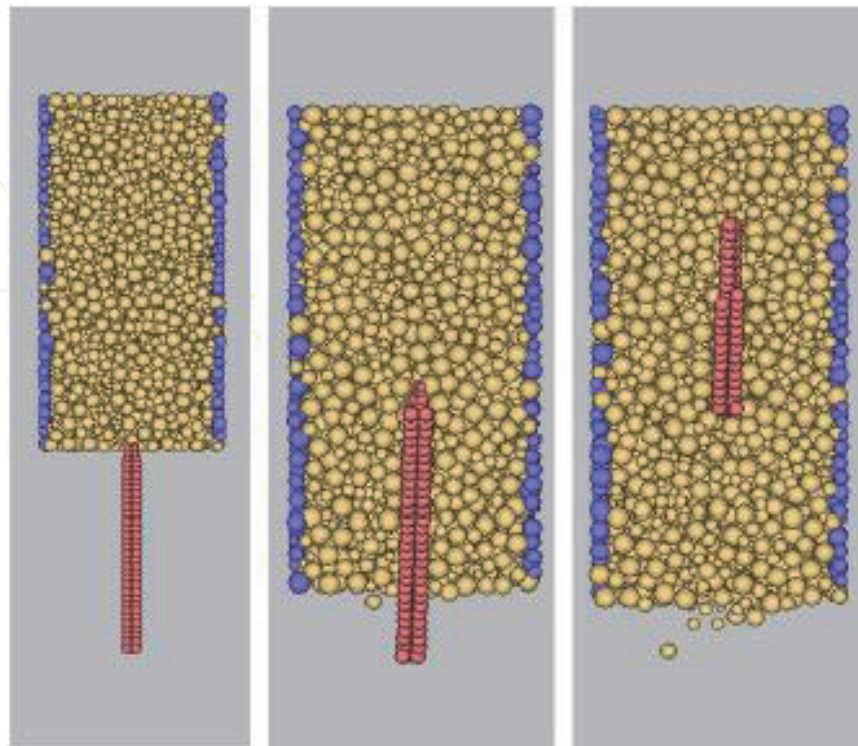

Figure 15.
Visualization of the penetration process using DEM (Zhou et al., 2009).

In the figure above, the concrete slab perforation process at selected time steps was initiated at a striking velocity of 500 m/s. Different steps correspond to different times, which can be obtained from the simulation history record. As shown, widespread cracking, progressive gross failure, and fragmentation during penetration can be visualized.

6. Conclusions

Penetration of projectile into concrete target was investigated in this research by using both experimental methods and numerical simulations. A lab test system which is able to launch steel projectile into cement concrete targets was successfully built. Projectile package driven by propellant gas enables a steel projectile to penetrate into cement concrete targets at different speeds. Finite Element Method (FEM) was utilized to simulate the penetration process of projectile into a concrete target. A projectile is considered as rigid material with no deformation during the penetration process. Cement concrete targets can be modeled using a concrete damaged plasticity model. Several major effects are estimated by FEM simulation including diameter, mass and initial speed of the projectile. Additionally, numerical simulation using Discrete Element Method (DEM) was employed to simulate the penetration process of projectile into cement concrete target. A calibration method was developed to obtain microscopic parameters from macroscopic parameters of concrete. Penetration process can be modeled using the time history of the depth, initial velocity and deceleration of the projectile then compare results with empirical predictions results of previously conducted simulations.

Author details

Cristian Druta
Virginia Tech Transportation Institute, Blacksburg, USA

*Address all correspondence to: cdruta1@vt.edu

IntechOpen

Compressive Strength of Concrete

References

[1] Iwama K, Higuchi K, Maekawa K. Multi-scale modelling of deteriorating concrete at elevated temperature and collapse simulation of underground ducts. In: 10th International Conference on Fracture Mechanics of Concrete and Concrete Structures FraMCoS-X. 2019

[2] Mehta PK, Monteiro PJM. Microstructure, Properties, and Materials. New York, London: The McGraw-Hill Companies, Inc.; 2006

[3] Roy DM, Idorn GM. Concrete Microstructure. In: Rep. SHRP-C-340, Strategic highway research program. Washington. D.C.: National Research Council; 1993

[4] Druta C, Wang L, Stephen Lane D. Tensile strength and paste-aggregate bonding characteristics of self-consolidating concrete. Construction and Building Materials. 2014;**55**:89-96

[5] Kuder K, Lehman D, Berman J, Hannesson G, Shogren R. Mechanical properties of self-consolidating concrete blended with high volumes of fly ash and slag. Construction and Building Materials. 2012;**34**:285-295

[6] Khayat KH, Guizani Z. Use of viscosity-modifying admixture to enhance stability of fluid concrete. ACI Materials Journal. 1997;**94**(4):332-340

[7] Ozyildirim C, Davis RT. Bulb-T beams with self-consolidating concrete on route 33 in Virginia. Journal of the Transportation Research Board. 2007;**2020**:76-82

[8] Gesoglu M, Guneyisi E, Ozbay E. Properties of self-compacting concretes made with binary, ternary, and quaternary cementitious blends of fly ash, blast furnace slag, and silica fume. Construction and Building Materials. 2009;**23**:1847-1854

[9] Castel A, Vidal T, Francois R. Bond and cracking properties of self-consolidating concrete. Construction and Building Materials. 2010;**24**:1222-1231

[10] Bijen JM, de Rooij M. Aggregate-matrix interfaces. In: Presented at International Conference on Concretes. Dundee, Scotland; 1999

[11] Herman G. Image Reconstruction from Projections: The Fundamentals of Computerized Tomography. New York: Academic Press; 1980

[12] Mindess S, Young JF, Darwin D. Concrete. Upper Saddle River, NJ 07458: Prentice Hall; 2003

[13] Hall C, Colston SL, Jupe AC, Jacques SDM, Livingston R, Ramadan AO. Non-destructive tomographic energy-dispersive diffraction imaging of the interior of bulk concrete. Cement and Concrete Research. 2000;**30**(3):491-495

[14] Shi BM, Wu Y, Chen Z, Inyang JH. Monitoring of internal failure evolution insoils using computerization X-ray tomography. Engineering Geology. 1999;**54**(3):321-328

[15] Rogasik HC, Wendroth JW, Young O, Joschko IM, Ritz MK. Discrimination of soil phases by dual energy X-ray tomography. Soil Science Society of America Journal. 1999;**63**(4):741-751

[16] Verhelst F, Vervoort ADB, Marchal G. X-ray computerized tomography, determination of heterogeneities in rock samples. In: Proceedings of the 8th International Congress on Rock Mechanics. Tokyo, Japan: A. A. Balkema; 1995. pp. 105-109

[17] Wang L, Frost JD, Shashidhar N. Microstructure study of westrack mixes

from X-ray tomography images. Journal of the Transportation Research Board. 2001;**1767**:85-94

[18] Wang L, Frost JD, Voyiadjis G, Harman TP. Quantification of damageparameters using X-ray tomography images. Journal of Mechanics and Materials. 2002;**35**: 777-790

[19] Cundall PA, Strack ODL. Discrete numerical model for granular assemblies. Geotechnique. 1979;**24**: 4843-4848

[20] Heuze FE. An overview of projectile penetration into geological materials, with emphasis on rocks. International Journal of Rock Mechanics and Mining Science and Geomechanics Abstracts. 1990;**27**(1):1-14

[21] Zhang D, Zhu F. Application of beam-particle model to the problem of concrete penetration. Explosion shock wave. 2005;**25**(1):85-89

[22] Kusano N, Aoyagi T, Aizawa J, Ueno H, Morikawa H, Kobayashi N. Impulsive local damage analyses of concrete structure by the distinct element method. Nuclear Engineering and Design. 1992;**138**(1):105-110

[23] Sawamoto Y, Tsubota H, Kasai Y, Koshika N, Morikawa H. Analytical studies on local damage to reinforced concrete structures under impact loading by discrete element method. Nuclear Engineering and Design. 1998; **179**(2):157-177

[24] Magnier SA, Donze FV. Numerical simulations of impacts using a discrete element method. Mechanics of Cohesive-frictional Materials. 1998;**3**(3): 257-276

[25] Ng T-T. Numerical Simulations for Penetration Process of Concrete Target Using the Discrete Element Method, New Orleans, LA, USA. New York, NY, USA: ASME; 1993, 1993

[26] Nishida M, Tanaka K, Matsumoto Y. Discrete element method simulation of the restitutive characteristics of a steel spherical projectile from a particulate aggregation. JSME International Journal Series A Solid Mechanics and Material Engineering. 2004;**47**(3):438-447

[27] Zhu F, Zhang D. Numerical simulation of perforation in plain concrete panel with nose shape of perforators. Journal Impact Factor. 2005;**24**:4843-4848

[28] Chen EP. Penetration into dry porous rock: A numerical study on sliding friction simulation. Theoretical and Applied Fracture Mechanics. 1989; **11**(2):135-141